Pertanika J. Sci. & Technol. 34 (5): 2619 - 2647 (2026)

PERTANIKA JOURNALS

SCIENCE & TECHNOLOGY

Journal homepage: http://www.pertanika.upm.edu.my/

Investigation of Assistive Grouser Traction Force in Toyoura Sand: Effects of Grouser Geometry and Contact Angle

Mochamad Edoward Ramadhan[1,2], Ahmad Najmuddin Ibrahim[2]*, and Yasuhiro Fukuoka[3]

[1]Department of Mechanical Engineering, Faculty of Engineering, University of Jember, Jalan Kalimantan No. 37, Tegalboto Campus, P.O. Box 159, Jember 68121, East Java, Indonesia
[2]Faculty of Manufacturing and Mechatronic Engineering Technology, Universiti Malaysia Pahang Al-Sultan Abdullah, Pekan Campus, 26600 Pekan, Pahang, Malaysia
[3]Department of Mechanical Systems Engineering, College of Engineering, Ibaraki University, 4-12-1 Nakanarusawa, Hitachi, Ibaraki 316-8511, Japan

ABSTRACT

Slip and sinkage remain critical challenges for wheeled robot mobility on granular terrain. Previous studies on assistive grousers have examined the effects of geometric shapes, while the orientation of the contact angle, which affects traction force generation, has not been investigated. This study investigated C-shaped (180°; C-Front: lateral face forward; C-Rear: lateral face rearward) and Chevron (120°) assistive grousers using kinematic analysis, force measurements with calibrated sensors, and force-time analysis during a single operating cycle. To determine the performance of the grouser-ground interaction, we conducted static resistance tests (100% slip) and dynamic traction tests (21-23% slip) on Toyoura sand using the Single-Wheel Test Bed (SWTB) under a 14 kg normal load at a rotational speed of 1 RPM. The C-Front configuration produced the highest forces (138.7 N resistance / 38.4 N traction), followed by C-Rear (57.1 N / 27.1 N), while Chevron yielded the lowest (44.0 N / 9.0 N). Despite having identical geometry, C-Front and C-Rear configurations differ significantly due to the orientation of the lateral side, which affects the geometric soil confinement mechanism. One-way ANOVA confirmed significant differences among all configurations ($p < 0.001$, $\eta^2 > 0.99$). Force-time analysis shows three phases: penetration, traction, and retraction, with different durations. C-Front exhibits the longest traction phase (38.95% of the cycle) compared with the Chevron configuration (28.36%). These results suggest that a smaller contact angle is more suitable for lightweight robots experiencing low

ARTICLE INFO

Article history:
Received: 26 June 2026
Accepted: 21 August 2026
Published: 30 October 2026

DOI: https://doi.org/10.47836/pjst.34.5.04

edoward.teknik@unej.ac.id (Mochamad Edoward Ramadhan)
anajmuddin@umpsa.edu.my (Ahmad Najmuddin Ibrahim)
yasuhiro.fukuoka.phd@vc.ibaraki.ac.jp (Yasuhiro Fukuoka)
* Corresponding author

e-ISSN: 2231-8526

© Universiti Putra Malaysia Press

resistance, while a forward lateral orientation maximises traction for heavier platforms in sandy terrain.

Keywords: Assistive grouser, bulldozing resistance, local traction, planetary rover, single wheel test bed

INTRODUCTION

In recent years, the mobility and traction performance of mobile platforms over unstructured or non-cohesive terrain have attracted significant research interest worldwide, particularly within European and global engineering frameworks. Reliable rover locomotion fundamentally depends on the contact mechanics between the propulsion system and the terrain, as well as the ability to avoid collisions with other objects in the surrounding environment; these are key requirements that wheeled robots must meet (Rubio et al., 2019).

Contact mechanics, the experimental basis for accurately measuring propulsion system performance related to tire-ground interface friction, remains a major challenge, requiring specialised instrumentation to accurately measure the friction coefficient. For example, the sliding friction parameter, which is strongly influenced by material properties such as contact surface roughness, humidity, lubrication, temperature, and relative velocity, remains a key parameter if environmental conditions can be determined (Kelemenová et al., 2020).

The ability to avoid collisions with other objects is essential for wheeled robots. Hruboš et al. (2016) used a 2-D scanner and utilised GPS and INS data fusion to create a final 3-D point cloud model. After generating the surface area, they applied textures automatically derived from a series of camera recordings. The final model was saved in *.obj format and consisted of individual environmental fragments that were then analysed for potential collisions with moving objects, which were then transferred through the measured environment. The term "moving object" could represent a train on a track or a vehicle on a road carrying a large load; environmental fragments searched for collisions could include trees, building parts, bridges, or power lines. The robotic manipulator developed by Blatnický et al. (2020), with a maximum load capacity of 25 kg for gripping automotive products, could also be used for evacuation to clear objects obstructing the rover's movement. It could also be used to lift the rover's body if its wheels become stuck in sandy terrain.

When combined with the robot’s inertial navigation system, which is equipped with an accelerometer and a gyroscope (Qazizada & Pivarčiová, 2016), the rover’s mobility system will be able to determine its position in space consistently and accurately. Considering the fundamental global progress and the research gaps still found in the development of wheel-mounted locomotion devices, this study focuses on wheels equipped with terrain-adaptive locomotion, which are the basis of rover mobility for exploration in all types of terrain.

In the field of Terramechanics, the efficient traversal of non-cohesive terrain is critical for the range and power autonomy of wheeled robots used in industrial, agricultural, and

aerospace exploration. The primary global challenges for these robots are slips and sinkage, which warrant detailed investigation (Tagliavini et al., 2022; Zhang et al., 2022). Soil displacement at the wheel-terrain interface occurs along longitudinal and lateral directions, inducing a bulldozing resistance that is a fundamental driver of slippage (Bekker, 1956; Wong, 1997). Watanabe et al. (2023) evaluated rigid-wheel dynamics under various conditions and identified critical trafficability thresholds. Furthermore, Sakayori and Ishigami (2024) confirmed that steady-state slip alters acting force as the terrain's load-bearing capacity fluctuates, compromising effective travel distance.

The development of sufficient tractive effort and soil shear strength is essential to mitigate these motion resistances. Classical frameworks by Bekker (1956) demonstrate that including grousers or spuds on rigid wheels facilitates soil densification, generating the thrust needed for translation while maintaining minimal slip ratios. To enhance predictions, Schäfer et al. (2010) modelled intricate wheel–soil dynamics, while Multi-Body System (MBS) frameworks, integrated with Soil Contact Models (SCM), enable sophisticated evaluations of sinkage and resistive forces. Notably, discrete grouser engagement typically induces sinusoidal oscillations in traction profiles. While conventional grousers can create voids that reduce traction (Yokoyama et al., 2020), trapezoidal shapes enhance performance by achieving superior soil compaction compared to rectangular designs (Suzuki et al., 2020). According to Nakamura et al. (2020), grouser integration fundamentally alters shear distributions, with the slip ratio increasing with increased vertical loading and diminished bearing capacity.

Research indicates that a 20° attack angle is optimal for maximising tractive effort on both level and sloped (0°-10°) granular terrain (Aziz et al., 2023). Experimental evaluations reveal that performance is primarily dictated by the number of grousers in active engagement with the substrate—which can cause fluctuating force profiles in multi-grouser setups due to mechanical interference—rather than the total count on the wheel (Aziz et al., 2023; Liu et al., 2024). To overcome these limitations, Ibrahim et al. (2016) introduced assistive grouser mechanisms with decoupled angular control to facilitate a consistent 0° angle of attack, defined throughout this study as the angle between the grouser blade and the vertical at the moment of soil entry, so that 0° denotes perpendicular penetration of the sand surface, resulting in improved efficiency and lower power consumption (Ibrahim & Fukuoka, 2018; Sabarudin et al., 2020a; Sabarudin et al., 2020b).

While Basri et al. (2024) established that expanding grouser width is ineffective in non-cohesive sand, grouser geometry and contact orientation remain critical for governing bulldozing resistance and soil translocation. This study specifically investigates the origins of negative traction forces (force reversals) identified in previous experimental data by comparing Chevron and C-shape designs within the assistive mechanism. Our methodology integrates kinematic analysis with the evaluation of calibrated load-cell signals to quantify how varying contact angles affect resistance and traction. These findings aim to provide

a comprehensive contribution to the development of high-traction assistive grousers for challenging terrains.

Kinematic Investigation and Trajectory Formulations

This kinematic model is the basis for the experimental design. Movement observations were modelled in two dimensions to interpret position changes relative to the wheel's movement (Figure 1). In the baseline conventional configuration, the U, V, and W grousers rotate by 30°. While grouser V aligns with the vertical axis at 270°—a position yielding maximum traction but inherent instability (Sutoh et al., 2012)—grousers U and W remain above the surface (Figure 1a). Unlike previous research focusing primarily on visualisation (Guo et al., 2021; Higa et al., 2016; Higa et al., 2019; Nakamura et al., 2020), this investigation analyses the full penetration-to-retraction cycle.

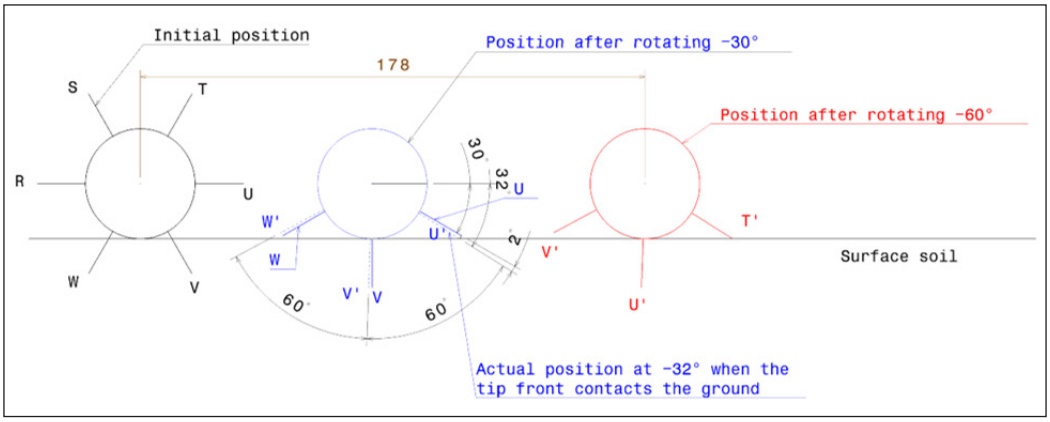

(a)

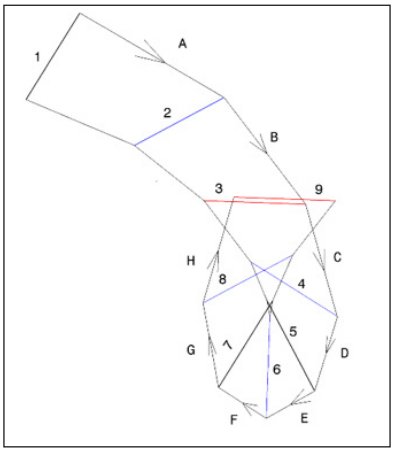

(b)

Figure 1. Motion of a conventional grouser (a) movement of the wheel with conventional grousers; (b) Trajectory of the grouser

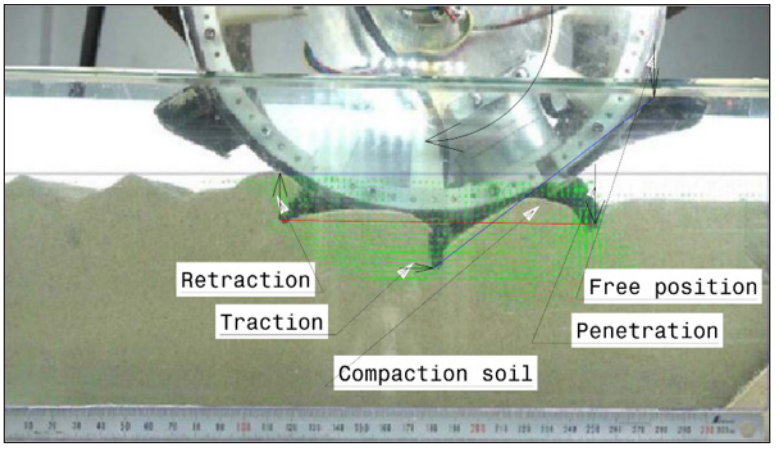

(a)

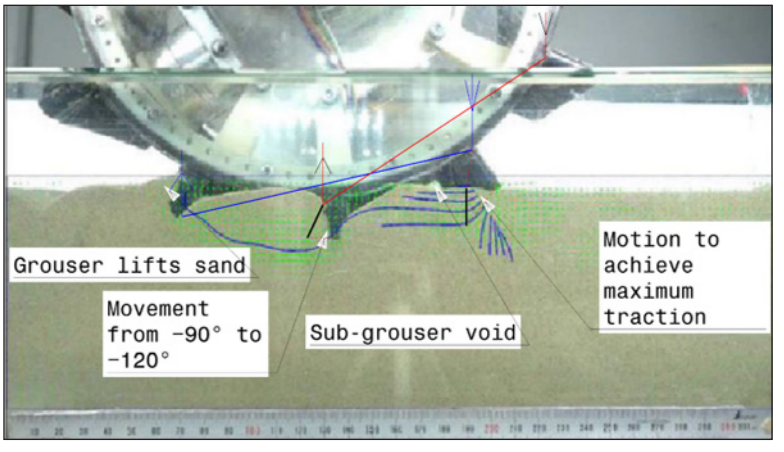

(b)

Figure 2. Motion of Conventional Grouser PIV (a) Grouser position; (b) Grouser motion (Nakamura et al., 2020)

Using the Particle Image Velocimetry (PIV) method (Nakamura et al., 2020), the unit progresses through six phases: surface movement (Phase C), initial penetration (Phase D), and maximum penetration (Phase E, 0°), where peak traction is generated. Steps following this peak are considered passive as the system converts torque into shear forces rather than effective displacement (F to H). Figure 2 illustrates the kinematic cycle of a conventional grouser, which has been revalidated through a kinematic investigation of a single grouser movement cycle (Figure 1b) involving eight analytical positions (A to H), where the 2 initial phases, A and B, are phases where the grouser does not interact with the ground. These trajectory positions can be obtained with smoother graphics using the following formulations: the translation of movement, Equations 1 and 2; wheel trajectory, Equations 3 and 4; and tip grouser formulations, Equations 5 and 6.

Translation of movement:

$$X_c(t_i) = X_0 - (R \times (\theta_i + \omega t_i) \times \frac{\pi}{180}) \quad [1]$$

$$Y_c = R \quad [2]$$

Trajectory of wheel formulation:

$$X_{wheel}(t_i) = X_c(t_i) + R\cos(\theta_i + \omega t_i + (k_{n-1}\frac{360}{\Delta\theta})) \times \frac{\pi}{180} \quad [3]$$

$$Y_{wheel}(t_i) = Y_c + R\sin(\theta_i + \omega t_i + (k_{n-1}\frac{360}{\Delta\theta})) \times \frac{\pi}{180} \quad [4]$$

Trajectory of tip grouser formulation:

$$X_{tip\ cg}(t_i) = X_c(t_i) + (R + L)\cos(\theta_i + \omega t_i + (k_{n-1}\frac{360}{\Delta\theta})) \times \frac{\pi}{180} \quad [5]$$

$$Y_{tip\ cg}(t_i) = Y_c + (R + L)\sin(\theta_i + \omega t_i + (k_{n-1}\frac{360}{\Delta\theta})) \times \frac{\pi}{180} \quad [6]$$

Where X_c is the x-coordinate of the axle position, X_o is the initial x-coordinate of the axle, θ_i is the initial contact angle of the wheel, ω is the angular velocity of the wheel, t_i is the time at the i-th step, R is the radius wheel in mm, Y_c is the y-coordinat of the axle position, X_{wheel} is the x-coordinate of the wheel, k_n is the n-th grouser, Y_{wheel} is the y-coordinate of the wheel, $\Delta\theta$ is the angle between grouser, $X_{tip\ cg}$ is the x-coordinate of the tip conventional grouser, $Y_{tip\ cg}$ is the y-coordinate of the tip conventional grouser, and L is length of grouser in mm.

In contrast, the assistive grouser mechanism (Ibrahim et al., 2016) utilises six grousers mounted parallel to one another and offset by −90° relative to the wheel radius, which maintains the 0° angle of attack defined above throughout soil engagement (Figure 3). This configuration ensures two grousers remain embedded, providing superior stability compared to perpendicular mountings (Demishkevich et al., 2025). The assistive grouser tip trajectory is calculated using equations 7 and 8. As shown in Figure 4, the mechanism enables simultaneous penetration, traction, and retraction, optimising work distribution and reducing energy consumption compared to conventional designs (Suzuki et al., 2020).

$$X_{tip\ ag}(t_i) = X_{wheel}(t_i) + R\cos(\theta_i + \omega t_i + (k_{n-1}\frac{360}{\Delta\theta})) \times \frac{\pi}{180} \quad [7]$$

$$Y_{tip\ ag}(t_i) = Y_{wheel} + (R\sin(\theta_i + \omega t_i + (k_{n-1}\frac{360}{\Delta\theta})) \times \frac{\pi}{180}) - H \quad [8]$$

Where $X_{tip\ ag}$ is the x-coordinate of the tip assistive grouser, $Y_{tip\ ag}$ is the y-coordinate of the tip assistive grouser, and H is the height of the assistive grouser in mm.

Both grouser mechanisms share the fundamental objective of generating a traction force and achieving a longitudinal displacement equivalent to the spacing between grousers. This functional goal, supported by Elsheikh (2023), is kinematically represented by the trajectories shown in Figure 4, derived from the formulations in Equations 1 through 8.

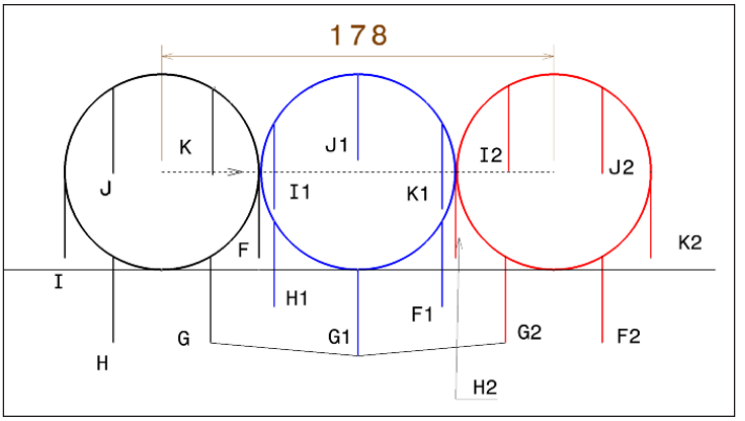

(a)

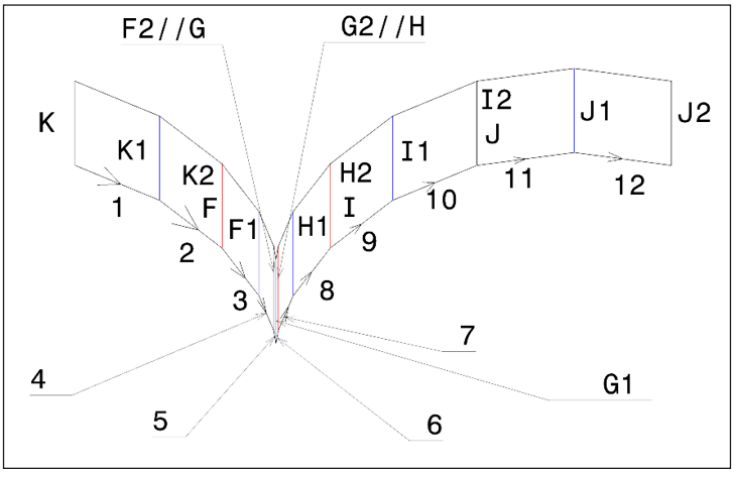

(b)

Figure 3. Motion of Assistive Grouser (a) Movement of the wheel with assistive grouser; (b) Trajectory of the assistive grouser

As illustrated in Fig. 6b, soil aggregation occurs predominantly along the front face of the C-Front grouser during translation. This aggregation phenomenon is governed by three primary physical drivers: first, the 180º concave lateral profile restricts lateral particle escape, forcing granular sand to compress inward. Second, continuous translation forces Toyoura sand along a bounded shear failure plane ahead of the grouser. Third, high localised shear displacement compresses soil particles into a dense state.

While internal particle velocity fields were not imaged dynamically via Particle Image Velocimetry (PIV) in this setup, the presence of geometric soil confinement is strongly supported by the post-test surface aggregation patterns (Figure 6b) and the sustained elevated force-time impulse profiles.

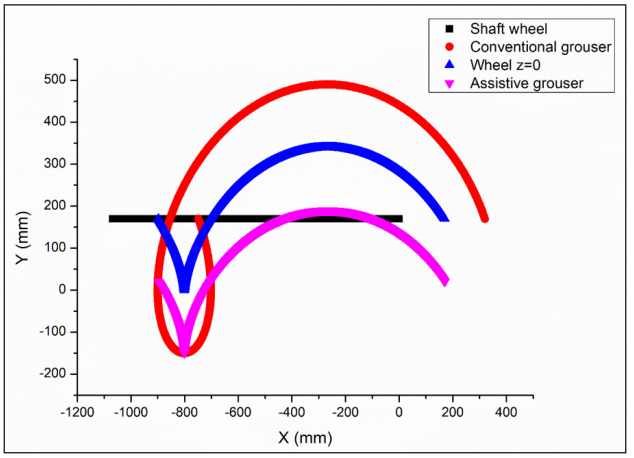

Figure 4. Comparison of trajectory

METHODOLOGY

Experimental Equipment and Substrate

To evaluate wheel-terrain interaction and tractive effort, this research employed a single-wheel test apparatus integrated into a laboratory test bed (Figure 5). The experimental wheel

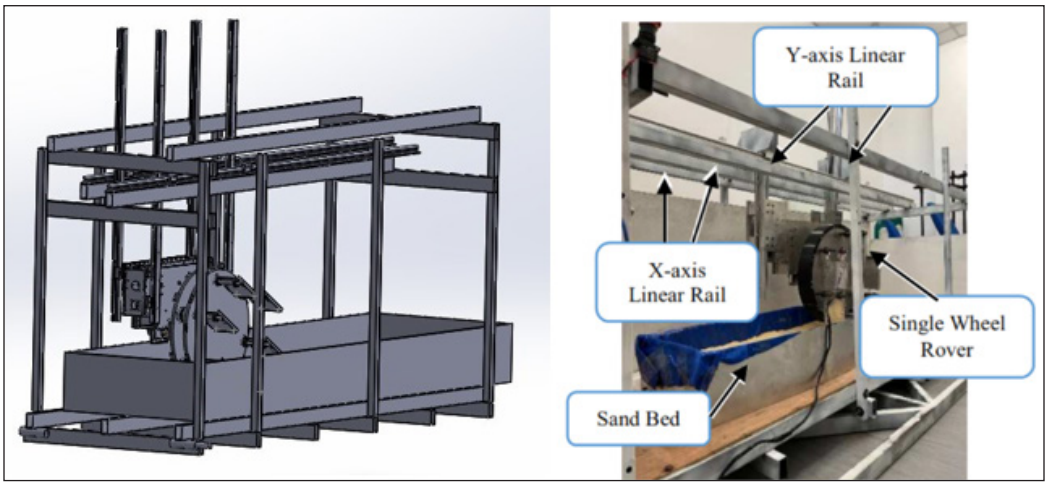

(a) (b)

Figure 5. Structural architecture (a) Design (b) Physical implementation of the single-wheel test apparatus

(radius: 205 mm, width: 60 mm) features a 6061-aluminium plate rim and a 3D-printed Poly Lactic Acid (PLA) structure. Based on a circumference division into 60º segments, the theoretical contact distance between consecutive grousers is 214.56 mm. The kinematic trajectory follows an arc length of up to 444 mm from soil entry to exit (Figure 6), with the support shaft fixed at a radius of 170 mm from the axle.

The soil bin facility (1000 × 250 × 160 mm) contained Toyoura sand maintained at a depth of 150 mm. The particle size of Toyoura sand typically ranges from 0.1 to 0.3 mm (Carow & Rackwitz, 2023; Ishikawa et al., 2014), with a bulk density between 1450 and 1600 kg/m³ (Onur et al., 2014), an internal friction angle between 32° and 46° (Safdar et al., 2021), and the cohesion is 0 kPa. To ensure environmental consistency, the laboratory was maintained at 26 °C and 60% humidity

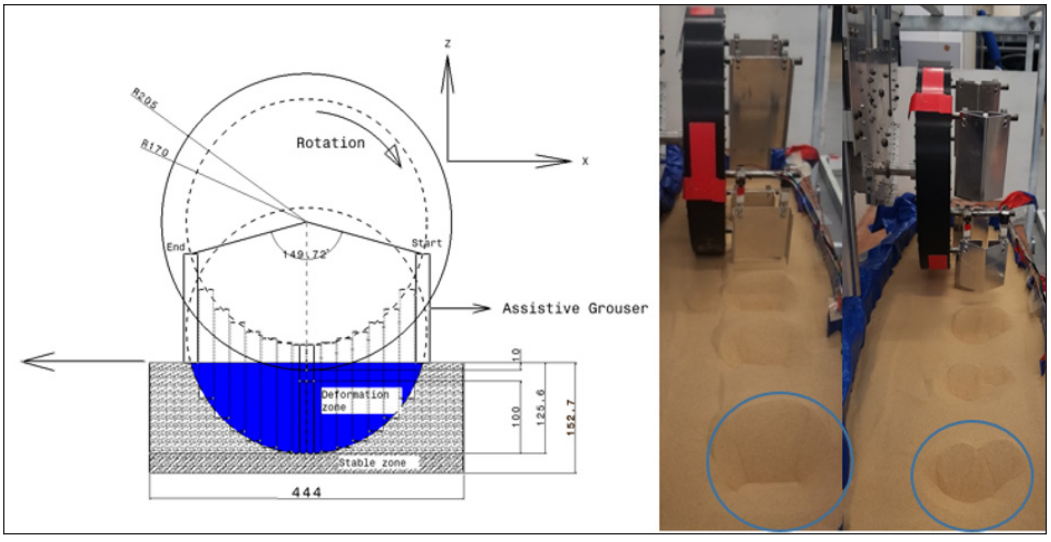

(a) (b)

Figure 6. Operational assessment of the assistive grouser through (a) Static loading and (b) dynamic cycle analysis

Grouser Morphology and Configurations

Drawing from Aziz et al. (2023) and Basri et al. (2024), we compared two 6061 aluminium alloy geometries (thickness: 2 mm, width: 90 mm, height: 100 mm):

- C-shaped: 180° inclusion angle (Figure 7a).
- Chevron-shaped: 120° inclusion angle (Figure 7b).

For the C-shaped profile, we evaluated two orientations: the forward-facing lateral configuration (C-Front) and the rearward-facing lateral configuration (C-Rear), as illustrated in Figure 8.

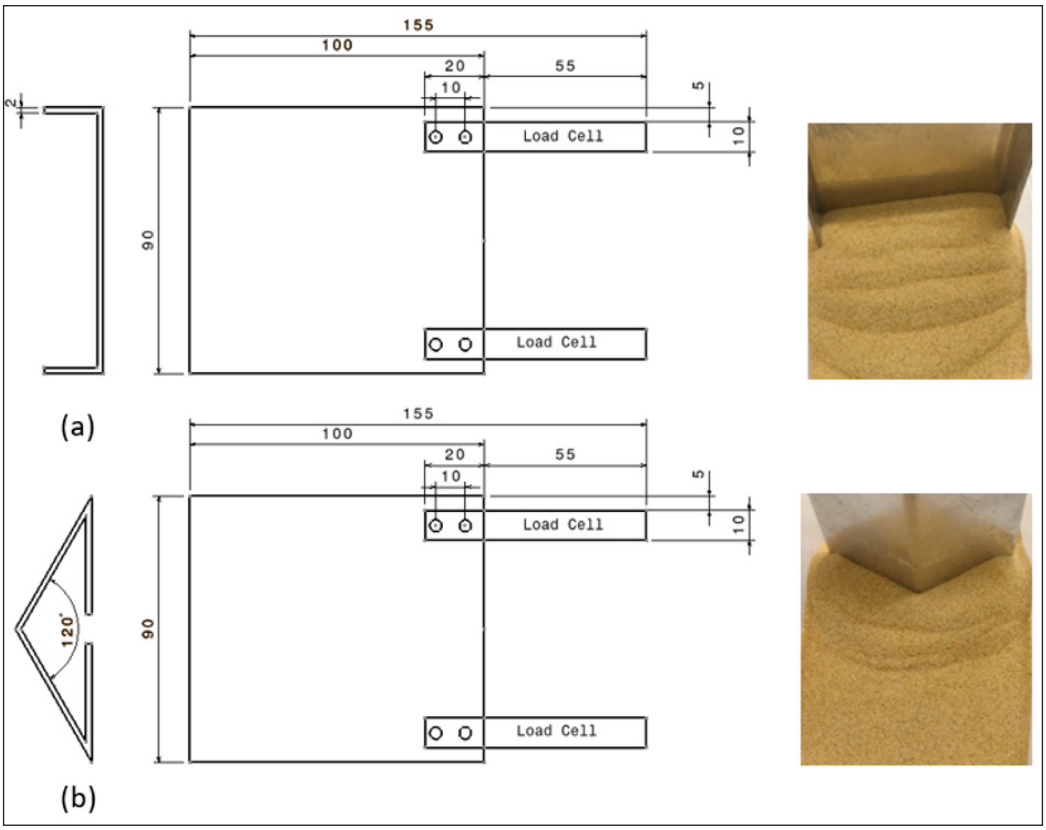

Figure 7. Integration and spatial placement of load cells within (a) C-shaped and (b) Chevron grouser assemblies

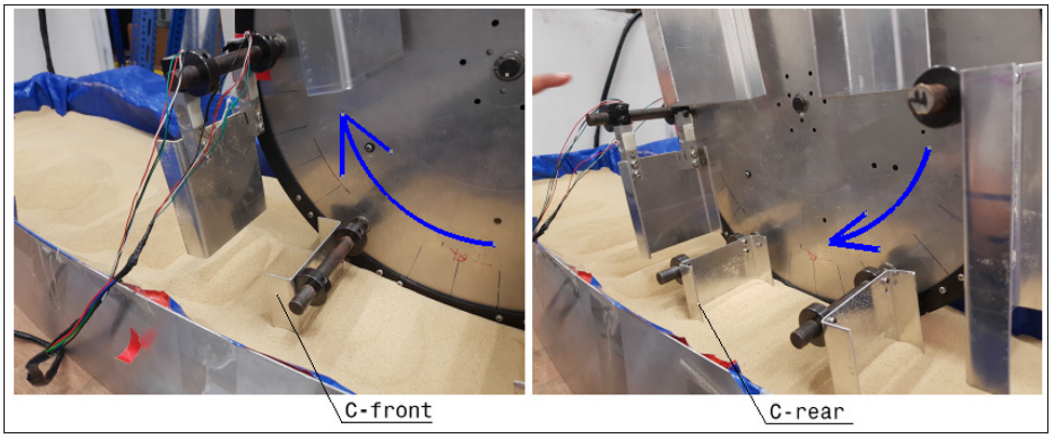

Figure 8. C-shape configuration

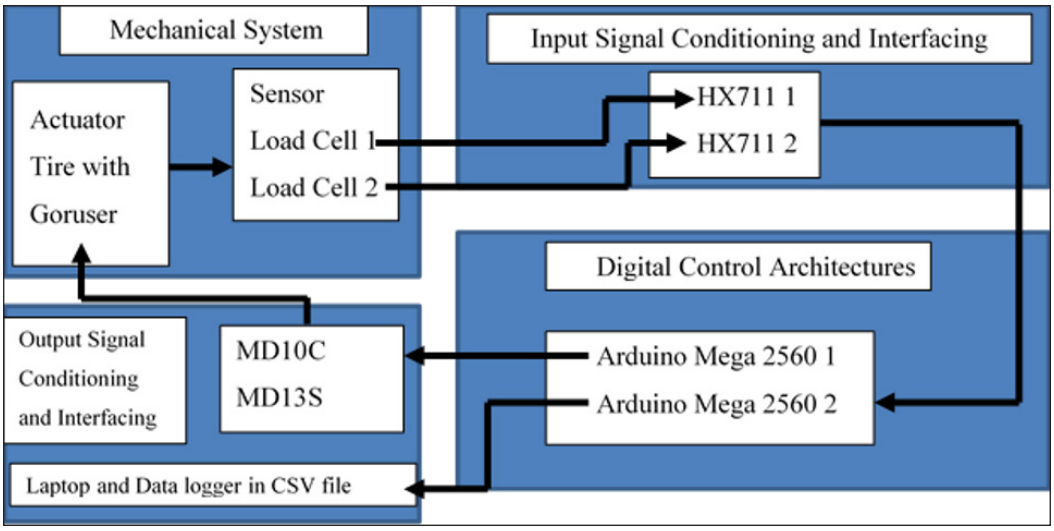

Figure 9. Integrated sensor architecture and motion control framework for force acquisition

Force Acquisition and Instrumentation

The data acquisition (DAQ) framework employs two 50-kg-capacity Load Cells (YZC-133, 0.05% FS) with HX711 converters and an Arduino Mega 2560 to manage signal flow for force measurement and motor actuation. Prior to testing, a 50 g (0.49 N) F2-class reference mass was used for zero-offset nulling and to verify signal sensitivity. Both load cells were mounted so that each responds to the full applied force, and the reported force is the mean of the two readings, (LC1 + LC2)/2. Averaging two independent measurements of the same load reduces random error and yields a single resultant estimate from two positions on the deflecting bracket. The same combination rule was applied throughout calibration, validation, and testing. Sensor accuracy was therefore determined empirically rather than assumed from the manufacturer's specification. Across the validated range of 0–10,000 g, the largest deviation of an individual cell was +40.78 g at 10,000 g, equivalent to 0.41% of reading or 0.082% of full scale, which exceeds the manufacturer's stated non-linearity tolerance of ±0.05% FS. The combined mean output, which is the quantity reported, deviated by +22.01 g at the same point, or 0.22% of reading and 0.044% of full scale, and therefore remains within that tolerance; averaging the two channels measurably improves accuracy relative to either cell alone. Measured accuracy is reported in place of the factory figure. The two channels differ by a mean of 38.2 g (SD 1.9 g) above 500 g while agreeing to within 0.12 g at 50 g, a behaviour consistent with a small seating effect in the Load Cell 2 mounting that is fully compensated by the individual calibration equations. The calibration factor disparity observed between Load Cell 1 (214.63 counts/g) and Load Cell 2 (219.03 counts/g) was due to slight strain-gauge manufacturing tolerances

and variations in mounting frame stiffness. To maintain high accuracy, each sensor was processed independently using its specific calibration equation (K_1 and K_2) rather than a single average value. Processed data are exported via USB in CSV format, while drive systems are manually operated. Theoretical tractive effort was determined by normalising axle torque against the respective radius equations 9 to 12. Peak forces during dynamic testing reached 40 N, well inside the directly validated range of 0-10,000 g (0-98 N). The peak static resistance of 138.7 N (≈14.1 kg) lies approximately 1.4 times beyond that range and rests on the fitted linearity of Equations 22 and 23 ($R^2 > 0.9999$); this extrapolation is acknowledged as a limitation of the static measurement.

$$\tau_{wheel} = \tau_{Elecric\ Motor} \times \text{Final Gear Ratio}_{Wheel} \quad [9]$$

$$F_{traction} = \tau_{wheel}(\text{Load or No-load}) \div r_{Wheel} \quad [10]$$

$$\tau_{Grouser} = \tau_{Elecric\ Motor} \times \text{Final Gear Ratio}_{Grouser} \quad [11]$$

$$F_{traction} = \tau_{Grouser}(\text{Load or No-load}) \div r_{Grouser} \quad [12]$$

Actuation and Transmission Systems

The system utilises 150W DC motors (Maxon RE40 series) with harmonic drive units. As detailed in Table 1 and Figure 10, the transmission architectures differ: the wheel employs a four-stage reduction (1088:1), while the assistive grouser uses a penta-stage configuration (1440:1). This "in-wheel" design places the shaft on the lateral side, allowing two grousers to maintain ground contact during rotation. During evaluation, the wheel moves along the longitudinal x-axis while the vertical z-axis remains unconstrained to account for dynamic sinkage. This substantial torque amplification (103.25 N.m for the wheel and 136.66 N.m for the grouser) guarantees continuous output velocity without speed fluctuation or stalling under peak passive bulldozing resistance (138.7N). Assuming the force vector is applied at the geometric centre of the wheel-ground interface with a distance of the wheel radius (0.205 m) and the assistive-grouser moment arm taken to the geometric centre of the 100 mm grouser blade (0.170 + 0.050 = 0.220 m), using formulas 10 and 12 yields an average gross tractive force of 503.66 N for the wheel and 621.18 N for the assistive mechanism.

Table 1
Drive System transmission specifications

Drive System	Stages	Total Ratio	Rated Output Torque (N.m)
Wheel	4 (2 × 100 × 1.7 × 3.2)	1088:1	103.25
Grouser	5 (2.5 × 100 × 1.44 × 2 × 2)	1440:1	136.66

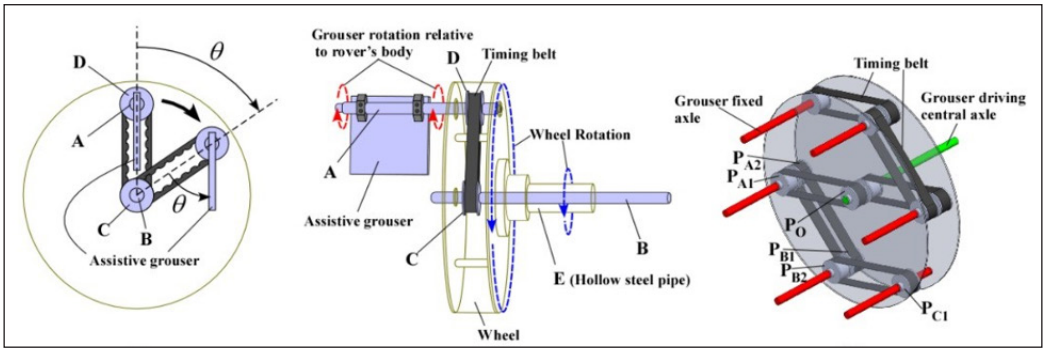

(a) (b) (c)

Figure 10. Wheel and assistive grouser transmission system (a) Angle between grousers; (b) Wheel shaft and grouser shaft; (c) Transmission for six grousers (Ibrahim et al., 2016)

Experimental Procedures

The sand was manually levelled before each trial to ensure a consistent terrain profile. Each run commenced with the wheel at the starting line and the instrumented grouser tip positioned 1–2 mm above the surface. The protocol followed two phases:

1. Static Calibration and Resistance: After zero-balancing the Load Cells, a 50-g F2-class weight was applied to derive scaling factors. Static resistance was then measured by rotating the grouser axle from 0° to -180 ° while the wheel was fixed.
2. Dynamic Testing: Tractive effort was characterised at 1 RPM, maintaining a 21%–23% slip ratio under a 14-kg normal load over a 170-mm displacement.

The Experimental baseline parameters- specifically, a normal vertical wheel load of 14 kg (137.34 N), a constant rotational speed of 1 RPM, and a dynamic slip ratio of 21-23% —were intentionally selected to represent the nominal operating profile of the target autonomous planetary rover. Operating at a low speed of 1 RPM enforces a quasi-static regime, eliminating inertial soil-throwing artefacts and enabling direct isolation of geometric contact forces.

RESULT AND DISCUSSIONS

This study examines the interaction between wheels equipped with an assistive grouser and Toyoura sand, focusing on quantifying resistive and resulting traction forces. Initially, the kinematic trajectories and operational dynamics of the assistive mechanism were benchmarked against traditional configurations to delineate fundamental differences between active decoupled systems and standard fixed-angle designs. Empirical evaluations show that C-shaped configurations, particularly in the C-Front orientation, generate the most significant resistive forces.

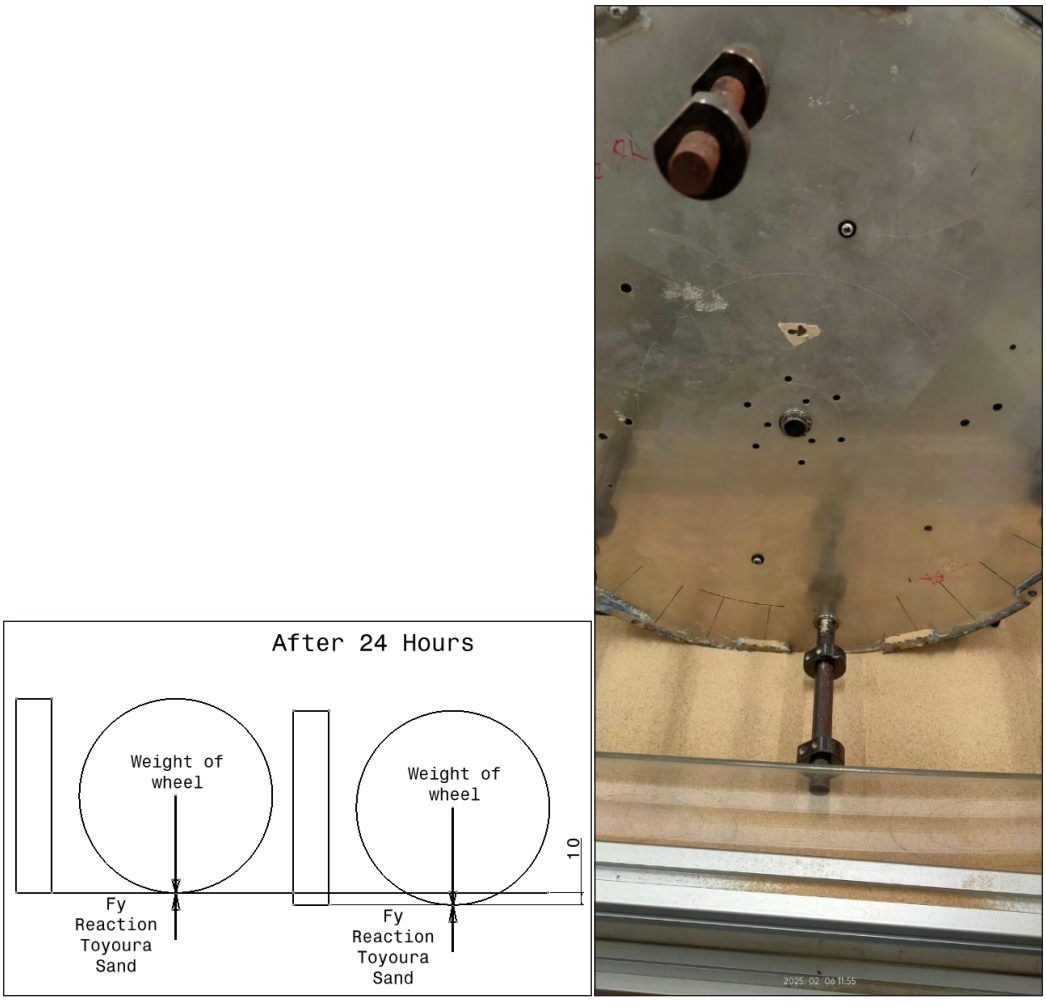

Figure 11. Static sinkage condition

Analysis of Static Sinkage and Baseline Bearing Capacity under Stationary Loading

This static test is a Bekker compression test used to determine the soil's bearing capacity under wheel loads. The difference is that the Bekker uses a single indenter and is pressed until the maximum downward movement is reached (due to applied pressure). While a stationary normal load of 14 kg (137.34 N) is applied to a natural substrate, where Newton's Third Law states that soil resistance must equal gravity in equilibrium (Boresi & Schmidt, 2001), wheel settlement results in an increasing surface area, encompassing both the underside and lateral areas. Unlike a rigid surface (W≤Soil bearing capacity), sand deforms and distributes pressure when the load exceeds its bearing capacity, causing the wheel to sink (W>Soil bearing capacity). After 24 hours of static loading, a 10 mm

settlement was observed (Figure 11). On the underside of the wheel tread and rim, the sand compacted downward from a narrow to a wide surface contact area, while in other areas, the sand deformed symmetrically toward the front, rear, and lateral surfaces of the wheel.

In conditions where the sinkage content changes from 0 to 10 mm against the wheel contact area, it can be mathematically determined using Equations 13 to 16, where Equations 13 and 14 define the symmetrical contact angle (θ0), Equation 15 gives the real curved contact area, and Equation 16 applies the wheel dimensions (R = 205 mm, B = 60 mm):

Symmetrical contact angle (θ_0)

$$\cos(\theta_0) = \frac{R-z}{R} = 1 - \frac{z}{R} \quad [13]$$

$$\theta_0 = arc\cos\ (1 - \frac{z}{R}) \quad [14]$$

Real curved contact area:

The total length of the curved contact arc from front to back is

$$A_{curved}\ = 2\,.B.R.arc\cos\ (1 - \frac{z}{R}) \quad [15]$$

Substitution of values R= 205 mm, B = 60 mm:

$$A_{curved}\ = 24600\ arc\cos\ (1 - \frac{z}{205})\ mm^2 \quad [16]$$

The area of the curve is the contact area where the soil bearing capacity is generated; this is evidence that the soil bearing capacity cannot be represented by an indenter in the form of a straight plate, as in a Bevameter.

Lateral contact area:

The lateral section consists of 2 flat, planar surfaces (the left and right sides of the wheel). The shape of the lateral contact area on each side is a circular sector with height z. Its area is given by Equation 17, and Equation 18 is obtained by substituting R = 205 mm.

$$A_{lateral}\ = 2\,.R^2.arc\cos\ (1 - \frac{z}{R}) - 2(R-z)\sqrt{2Rz - z^2} \quad [17]$$

Substitution of values R = 205 mm:

$$A_{lateral}\ = 84050\,.arc\cos\ (1 - \frac{z}{205}) - (410 - 2z)\sqrt{410z - z^2}\ (mm^2) \quad [18]$$

Note: The angle arc cos must be calculated in radians.

Total Wheel-to-Ground Surface Contact Area (A_{total}) z = 10 mm:

$$A_{total} = A_{curved} + A_{lateral} = 7715\,mm^2 + 1695\,mm^2 = 9410\,mm^2 \quad [19]$$

$$\sigma_{vertical} = \frac{W}{A_{Curved}} = \frac{137.34\,N}{7715\times10^{-6}m^2} = 17.80\,kPa \quad [20]$$

$$\sigma_{lateral} = \frac{A_{lateral}}{A_{curved}} \times \sigma_{vertical} = \frac{1695}{7715} \times 17.80 = 3.91\,kPa \quad [21]$$

At z = 10 mm, the total contact area is 9410 mm² (Equation 19), giving a vertical normal pressure of 17.80 kPa (Equation 20) and a lateral pressure of 3.91 kPa (Equation 21). Normal pressure is greatly influenced by the wheel's immersion and sinkage. The deeper the contact area, the larger it is, resulting in a smaller normal pressure. This corresponds to the soil's bearing capacity for the wheel's weight at rest. Meanwhile, when the wheel is at rest, the lateral side of the wheel also experiences uniform pressure, so the magnitude of the wheel's lateral pressure is the ratio of the lateral area to the bottom's curved area, producing normal pressure.

Evaluating the Magnitude of Soil Resistance Forces via Calibrated Instrumentation

Digital output profiles from the HX711 converters under idle and loaded states are illustrated in Figure 12. Raw ADC signals maintained a steady baseline with minimal noise (±50 counts) until the 22-second mark, where load application triggered a step-rise peaking at

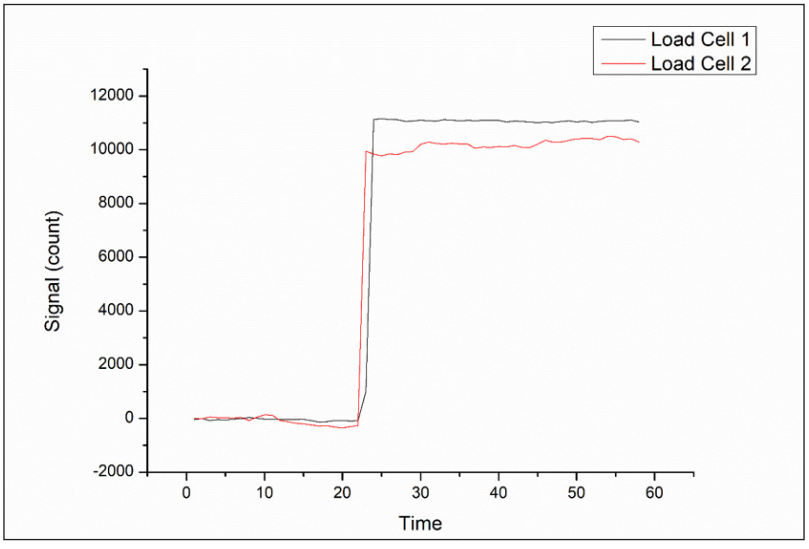

Figure 12. Raw ADC signal response of HX711 converters under no-load and applied-load

11,128 counts (Load Cell 1) and 9,953 counts (Load Cell 2). While Load Cell 2 responded approximately 1 second faster, Load Cell 1 demonstrated higher sensitivity, confirming the hardware's precision in force measurement.

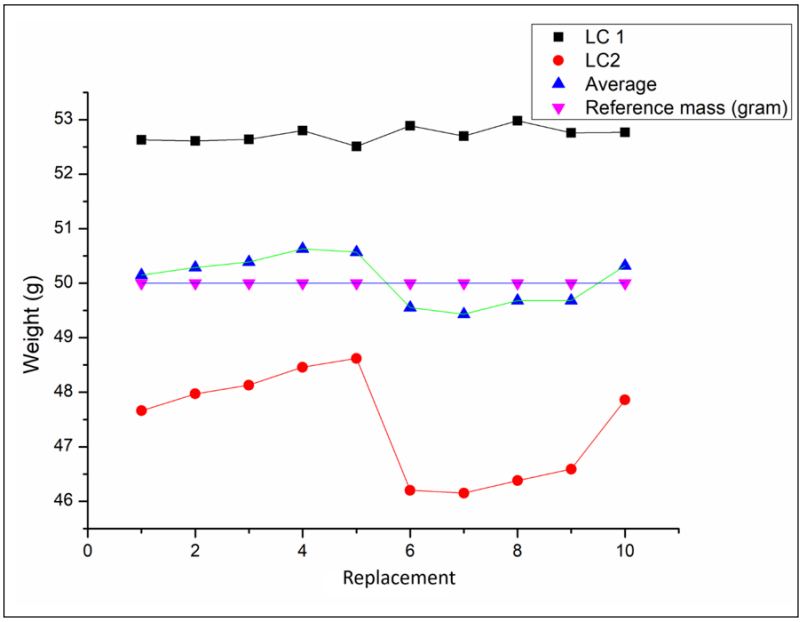

Figure 13. Systematic calibration and performance verification of the dual load cell assembly

To ensure system precision, calibration was performed using a 50 g F2-class standard weight. Across ten iterative trials, the system derived scale factors of 214.63 (LC1) and 219.03 (LC2), with integrated outputs ranging between 49.42 and 50.63 g. Statistical analysis verified the instrumentation's accuracy, yielding a mean deviation of +0.06 g (SD: 0.45 g, $p = 0.65$). As depicted in Figure 13, a detailed analysis of the calibration dataset revealed a shift in performance between the initial five trials (mean deviation: +0.40 g) and the subsequent five (mean deviation: -0.27 g). This variance was primarily caused by localised underestimation in Load Cell 2 during trials 6 through 9, which showed drops ranging from -0.32 g to -0.58 g. These deviations in Load Cell 2 readings stem from manufacturing tolerances and variations in mounting stiffness and are compensated for by applying individual Load Cell calibration factors rather than a combined average value. Despite these minor fluctuations, the absolute measurement error remained consistently below 1 g throughout the process, confirming high accuracy for subsequent dynamic testing. To ensure the accuracy of the Load Cell readings, a validation process is performed using the F2 standard over the range 0 to 10,000 grams, as shown in Table 2.

Table 2
Validation Mass balance 0-10,000 grams

Mass balance F2 (gram)	LC 1(gram)	LC 2 (gram)	Average (gram)
0	0	0	0
50	50.06	49.94	50.00
100	123.28	79.81	101.55
500	516.18	477.16	496.67
1000	1019.72	981.4	1000.56
2000	2020.81	1984.36	2002.59
3000	3019.32	2978.3	2998.81
4000	4020.56	3984.81	4002.68
5000	5021.24	4983.2	5002.22
6000	6021.56	5982.92	6002.24
7000	7026.85	6990.54	7008.69
8000	8023.45	7985.92	8004.68
9000	9028.42	8990.26	9009.34
10000	10040.78	10003.24	10022.01
Average (3975)	3995.16	3962.28	3978.72

The validation data in Table 2 were fitted by least-squares linear regression of the form Y = a + bX, where X is the F2 reference mass and Y is the load cell reading (g). The resulting calibration equations for Load Cell 1 and Load Cell 2 are given in Equations 22 and 23, respectively, and both show near-perfect linearity (R^2 = 0.99998 and 0.99999). The fitted lines against the F2 standard are plotted in Figure 14.

$$Y = a + b.X$$

Load Cell 1

$$b1 = \frac{\sum(Xi - 3975)(Y1i - 3995.16)}{\sum(Xi - 3975)^2} = 1.0022$$

$$a1 = \bar{Y} - b1.\bar{X} = 3995.16 - (1.0022 \,.\, 3975) = 11.32 \qquad [22]$$

$Y1 = 11.32 + 1.0022X$, R^2 = 0.99998

Load Cell 2

$$b2 = \frac{\sum(Xi - 3975)(Y2i - 3962.28)}{\sum(Xi - 3975)^2} = 1.0006$$

$$a2 = \bar{Y} - b2.\bar{X} = 3962.28 - (1.0006 \,.\, 3975) = -15.11 \qquad [23]$$

$Y2 = -15.11 + 1.0006\,X$, R^2 = 0.99999

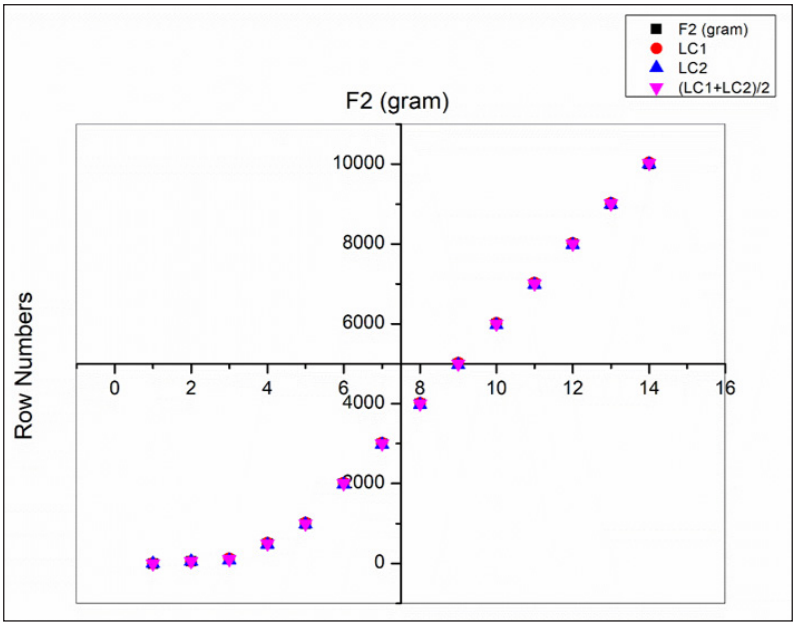

Figure 14. Validation Load Cell 1 and Load Cell 2 with F2 standard

Characterising Total Resistive Forces across Diverse Grouser Geometries and Contact Orientations

To characterise static soil resistance, the experimental procedure involves holding the wheel in a fixed state while rotating the assistive grouser axle from 0° to 180°. To ensure data reliability across 10 retrieval cycles, the displaced sand is manually flattened, and a wheel retainer is reinstalled before each trial. Bekker's original sand shear force measurements, which involved moving a rectangular plate in the longitudinal direction, could only measure the maximum force separately. Due to limitations in constructing a mechanism to approximate the cycloidal motion of the grouser, we measured the maximum shear force by rotating it half a rotation, with the goal of recording all shear forces generated by the grouser and the sand during its interaction.

As illustrated in Figure 15, the contact area angle is a decisive factor; geometric differences result in a reduction in resistive force of approximately 22.9% between C-Rear and Chevron. Statistical analysis using one-way ANOVA confirms that these differences are highly significant ($p < 0.001$, $\eta^2 = 0.999$), with the C-Front configuration yielding the highest average total resistance force at 138.7 N, followed by C-Rear (57.1 N) and Chevron (44.0 N), as detailed in Table 3. The one-way ANOVA results are summarised in Table 4, and the post-hoc Tukey HSD comparisons in Table 5 confirm that all three pairwise differences are significant ($p < 0.001$).

Table 3
Resistance force

Replication	C-Front (N)	C-Rear (N)	Chevron (N)
1	140	59	43
2	136	56	42
3	139	57	45
4	140	57	44
5	137	59	44
6	140	55	45
7	139	57	43
8	142	57	44
9	138	55	46
10	136	59	44
	Mean (N)	**SD (N)**	**SE (N)**
C-Front	138.7	1.95	0.62
C-Rear	57.1	1.52	0.48
Chevron	44.0	1.15	0.36

Table 4
One-way ANOVA of resistance force

Source of Variation	SS	df	MS	F	p-value
Between Groups	52661.0	2	26330.5	10611.0	<0.001
Within Groups	67.0	27	2.48	-	-
Total	52728.0	29	-	-	-

Table 5
Post-Hoc tukey HSD of resistance force

Comparison	Mean Difference (N)	p-value	Conclusion
C-Front vs C-Rear	+81.6	<0.001	Significant
C-Front vs Chevron	+94.7	<0.001	Significant
C-Rear vs Chevron	+13.1	<0.001	Significant

These measurements provide evidence that the total resistance force generated by each configuration with the same surface area differs in the direction of flow and in sand compaction, significantly affecting the resulting total resistance force, regardless of whether the surface area is tangential or lateral. In a 100% slip condition, the measured soil shear force equals the total resistance force, and it must be less than the net traction force. The net traction force is obtained from Equation 24 by subtracting the measured total resistance force from the gross tractive force of the assistive grouser shaft (621.18 N), giving 482.48 N for C-Front, 564.08 N for C-Rear and 577.18 N for Chevron as shown in Equations 25 to 27.

$$F_{net} = \tau_{shaft\ grouser} - Total\ Resistance\ Force \quad [24]$$

$$F_{net}\, C - Front = \frac{136.66\ N.m}{0.170\ m + 0.050\ m} - 138.7\ N = 482.48\ N \quad [25]$$

$$F_{net}\, C - Rear = \frac{136.66\ N.m}{0.170\ m + 0.050\ m} - 57.1\ N = 564.08\ N \quad [26]$$

$$F_{net}\, Chevron = \frac{136.66\ N.m}{0.170\ m + 0.050\ m} - 44.0\ N = 577.18\ N \quad [27]$$

This behaviour is theoretically grounded in the superposition principle of Granular Resistive Force Theory (GRFT), as proposed by Treers et al. (2021), which posits that the orientation of surface elements relative to the motion vector alters interaction patterns. Specifically, the forward lateral orientation of the C-Front design traps and accumulates sand, whereas the backward orientation of the C-Rear allows soil to flow toward the sides. These findings align with the classical theory of passive soil pressure, characterising clean Toyoura sand as having stable, high cumulative resistance at 100 mm penetration depths with minimal particle movement. Furthermore, the results corroborate research by Suzuki et al. (2020) regarding the functional tradeoff between resistive force magnitude and sinkage across different geometries.

Influence of Divergent Grouser Contact Angles on Tractive Effort Generation within Granular Media

Slip range of 21-23% at an angular speed of 1 RPM, it turns out that the need for soil shear force to hold the grouser to produce traction force on the assistive grouser mechanism with an angle of attack of 0 degrees, with a grouser height area of 100 mm, with 3 configurations, turns out to be smaller than static testing, assuming 100% slip occurs. The magnitude of the traction force equivalent to the soil shear force is reported as follows: according to the results visualised in Figure 16, the C-Front layout generates the highest maximum soil shear force at 38.4 N. In comparison, the C-Rear arrangement provides the next performance tier with a peak traction of 27.1 N. Statistically, this performance gap is highly significant ($p<0.001$), with the C-Front producing approximately 42% more traction than the C-Rear and 4.3 times as much as the Chevron design. Even the C-Rear configuration demonstrated a superior response, yielding nearly three times the force recorded for the Chevron system (9.0 N), with a detailed breakdown presented in Table 6. The one-way ANOVA results for tractive effort are summarised in Table 7 ($\eta^2 = 0.997$), and the post-hoc Tukey HSD comparisons in Table 8 confirm that all pairwise differences are significant ($p < 0.001$).

Table 6
Tractive effort

Replicate	C-Front (N)	C-Rear (N)	Chevron (N)
1	38	27	9
2	39	26	10
3	37	27	9
4	39	27	10
5	39	28	9
6	38	26	8
7	39	27	10
8	39	28	8
9	38	27	9
10	38	28	8
	Mean (N)	**SD (N)**	**SE (N)**
C-Front	38.4	0.7	0.22
C-Rear	27.1	0.74	0.23
Chevron	9.0	0.82	0.26

Table 7
One-way ANOVA of tractive effort

Source of Variation	SS	df	MS	F	p-value
Between Groups	4399.2	2	2199.6	3880.0	<0.001
Within Groups	15.3	27	0.57	-	-
Total	4414.5	29	-	-	-

Table 8
Post-Hoc Tukey HSD of tractive effort

Comparison	Mean Difference (N)	p-value	Conclusion
C-Front vs C-Rear	+11.3	<0.001	Significant
C-Front vs Chevron	+29.4	<0.001	Significant
C-Rear vs Chevron	+18.1	<0.001	Significant

These significant disparities are primarily attributed to the orientation of the lateral faces. Specifically, the forward-facing edges of the C-Front design facilitate a robust soil-trapping and compaction mechanism within the Toyoura sand, enabling the mechanism to collect and move soil particles more effectively than the more streamlined Chevron geometry.

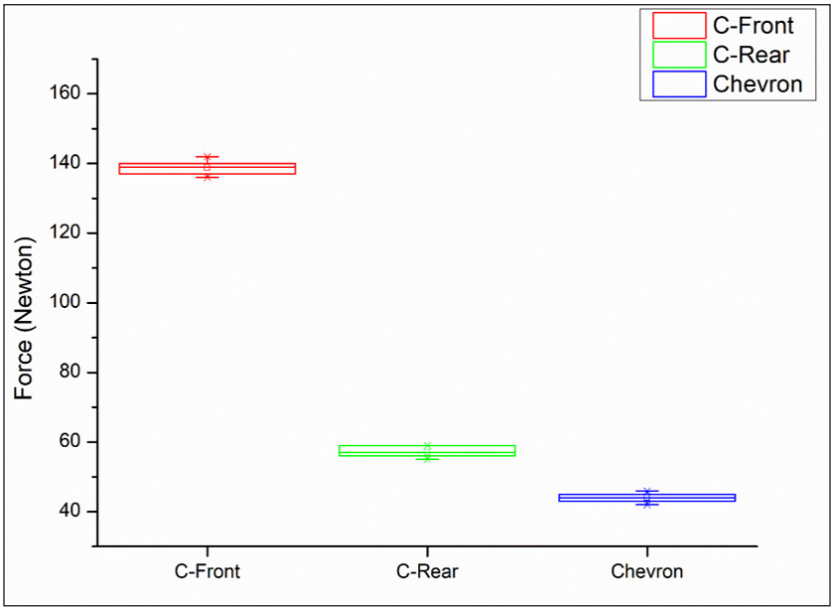

Figure 15. Peak resistive force response in Toyoura sand during static loading trials

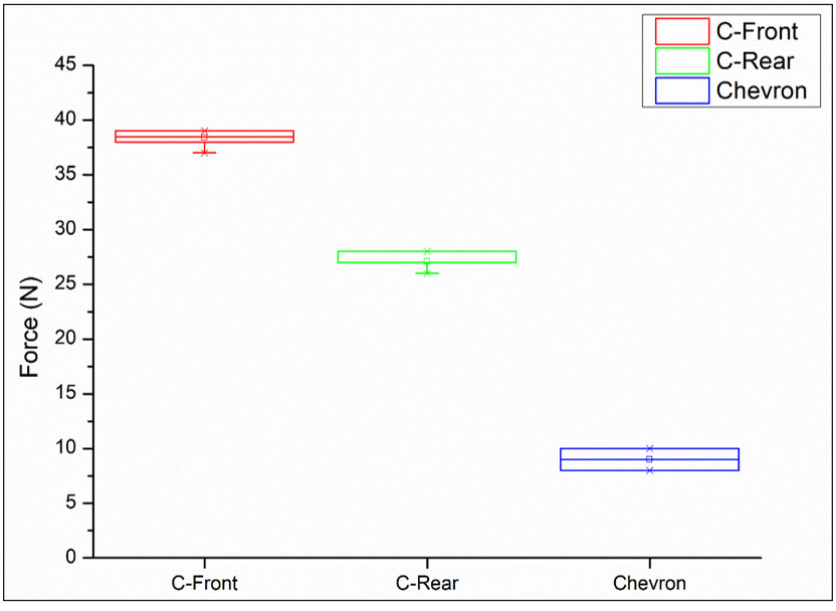

Figure 16. Magnitude of localised traction force development in Toyoura Sand

This research corroborates the findings of Aziz et al. (2023) on the role of contact angles while introducing critical methodological improvements. Unlike previous studies that lacked environmental controls, this investigation maintained a temperature of 26±1°C

and humidity of 60±2% to prevent moisture-induced pseudo-cohesion from affecting soil shear strength (Tapia et al., 2016). By implementing these rigorous controls and calibrated measurements, this study provides a more accurate and reliable data set than earlier reports based on raw values.

From both static tests with 100% slip and natural dynamic tests with 21-23% slip, it can be concluded that the traction force is generated by the grouser through shear-force compaction (tangential) and soil-bearing capacity (normal), without exceeding the total resistance force. If it exceeds that, the sand flows from beneath the wheel surface and collects behind the wheel.

Comprehensive Analysis of Force-Time Profiles Throughout the Assistive Grouser Operational Cycle

The advantage of using two Load Cells placed on one grouser is its ability to report the grouser deflection movement due to soil shear forces during the clockwise test. While previously assumed to be driven only from behind the wheel (in front of the grouser in its direction of travel), it turns out that the sand in front also contributes to generating traction force. The values derived from the force-time analysis represent instantaneous peak values from a single representative cycle, rather than trial averages.

The force-time history across all geometries reveals a consistent tri-phase cycle—penetration, traction generation, and retraction—within a 19-second operational window as reported in Figure 17. The penetration phase (6.0–6.4 s) is temporally uniform, though peak forces vary significantly: C-Front (+38 N), C-Rear (+28 N), and Chevron (+8 N), with all peaks occurring between the 3 and 4-second marks. These findings expand upon Aziz et al. (2023) by quantifying the interplay between contact angles and tractive effort through calibrated instrumentation.

During the traction phase, tractive effort increases progressively, peaking at −35 N for the C-Front, compared to −20 N (C-Rear) and −10 N (Chevron). This performance is driven by a superior soil-trapping mechanism—characterised by forward-facing lateral edges—that facilitates more effective soil collection and compaction. This mechanism not only increases force magnitude but also extends traction persistence; the phase duration expanded from 28.36% (Chevron) and 32.26% (C-Rear) to a maximum of 38.95% for the C-Front. This increased persistence enables the C-Front to dominate the net impulse, ensuring robust mobility on granular substrates such as Toyoura sand.

Experimental results registered positive penetration impulses of +26.5 N.s (Chevron), +83.2 N.s (C-Rear), and +112.4 N.s (C-Front). The peak negative impulse—representing the tractive effect as the grouser engages the substrate—was most pronounced in the C-Front design (−153.1 N.s), followed by the C-Rear (−50.0 N.s) and Chevron (−24.3 N.s). The net impulse generated by the C-Front was −40.7 N.s, followed by the Chevron

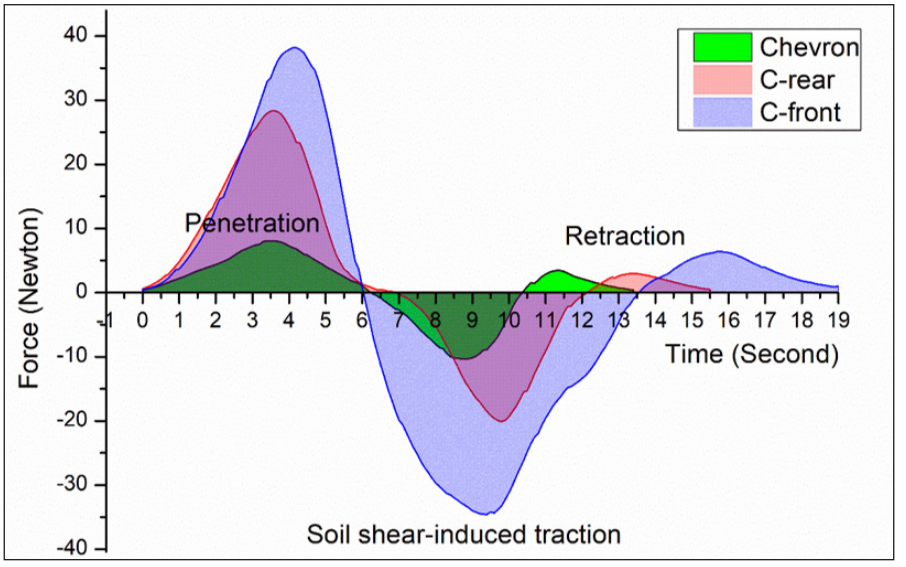

Figure 17. Sequential three-phase operational cycle of the assistive grouser mechanism

and C-Rear configurations of +2.2 N.s and +33.2 N.s, respectively, facilitating smoother forward motion.

The maximum change in position, with a value of + to -, is the magnitude of the generated traction force, which is the average value of the total amplitude formed by one cycle because of the interaction of the sheer force of the sand in front of and behind the grouser.

These disparities highlight unique force-response patterns within a single wheel–ground interaction cycle. The C-Front configuration excels at initial penetration and generates sustained traction, but it also triggers significant densification and shear failure in the granular material. This behaviour aligns with Terramechanics principles, in which increased effective contact area reinforces soil slice formation while elevating compaction resistance and energy dissipation. Conversely, the Chevron and C-Rear designs exhibit lighter ground interactions; while their peak forces are lower, they facilitate a faster release of granular material, optimising efficiency.

Ultimately, these findings underscore a fundamental trade-off between maximum penetration capacity and force-generation efficiency. An optimal assistive grouser must balance aggressive soil engagement with the ability to efficiently release compacted materials, a critical factor for wheeled robot mobility in granular terrain like Toyoura sand.

CONCLUSION

This study demonstrates that assistive grouser geometry, specifically contact angle and orientation, significantly dictates traction performance on Toyoura sand. The C-Front

configuration (180° angle, forward-facing) proved most effective, generating a peak traction force of 38.4 N by forming a robust passive soil wedge. In contrast, the C-Rear and Chevron geometries produced lower forces (27.1 N and 9.0 N, respectively), a disparity confirmed as highly significant ($p<0.001$). Force-time analysis identified a consistent tri-phase interaction:

- Penetration: Lasting 6.0–6.4 s, with the C-Front reaching a peak force of +38 N.
- Traction: The C-Front maintained the highest persistence, occupying 38.95% of the cycle compared to only 28.36% for the Chevron.
- Retraction: All geometries exhibited force restoration as soil was displaced toward the surface.

These results highlight a fundamental mechanical trade-off: aggressive designs like the C-Front maximise soil engagement but increase compaction resistance, resulting in a negative local net impulse (−40.7 N.s). However, the assistive mechanism's independent angle control ensures that the overall system's mobility remains superior to that of conventional designs. Optimising the balance between aggressive engagement and efficient material release is essential for traversing granular terrain. These findings establish design guidelines for high-traction wheels. Future work will extend the evaluation across multiple normal loads and rotational speeds and across the full slip curve from 0% to 100%, rather than the single operating point examined here, and will apply Particle Image Velocimetry particle tracking to image the internal soil velocity field directly, so that the geometric soil confinement mechanism inferred in this study can be confirmed by observation of soil flow rather than by force response alone.

ACKNOWLEDGEMENT

The authors would like to thank the Ministry of Higher Education Malaysia for financial support under the Fundamental Research Scheme (FRGS) No. FRGS/1/2023/TK10/UMP/02/37 (University reference RDU230135), Ministry of Education Malaysia, Ministry of Education Indonesia, University of Jember, and Universiti Malaysia Pahang Al-Sultan Abdullah for the facilities and support provided for this research.

LIST OF ABBREVIATION

SWTB	Single-Wheel Test Bed
2-D	Two-Dimensional
GPS	Global Positioning System
INS	Inertial Navigation System

3-D	Three-Dimensional
ANOVA	Analysis of Variance
CCD	Continuous Collision Detection
MBS	Multi-Body System
SCM	Soil Contact Models
PIV	Particle Image Velocimetry
PLA	Poly Lactic Acid
DAQ	Data Acquisition
USB	Universal Serial Bus
CSV	Comma-Separated Values
ADC	Analog-to-Digital Converter
LC	Load Cell
GRFT	Granular Resistive Force Theory
RPM	Revolutions Per Minute
FRGS	Fundamental Research Scheme

REFERENCES

Aziz, I. N. A. C., Ibrahim, A. N., Basri, I., & Fukuoka, Y. (2023). Rover wheel assistive grouser angle of attack effects on traction force in soft terrain. In *2023 19th IEEE International Colloquium on Signal Processing & Its Applications (CSPA)* (pp. 236-241). IEEE. https://doi.org/10.1109/cspa57446.2023.10087721

Basri, I., Aziz, I. N. A. C., Ibrahim, A. N., & Fukuoka, Y. (2024). Investigation of wheel robot grouser width parameter effect on robot mobility in soft sand terrain using sand test bed. In W. H. Mohd. Isa, I. M. Khairuddin, M. A. Mohd. Razman, S. Saruchi, S. H. Teh, & P. Liu (Eds.), *Intelligent manufacturing and mechatronics* (Vol. 850, pp. 199-207). Springer. https://doi.org/10.1007/978-981-99-8819-8_16

Bekker, M. G. (1956). *Theory of land locomotion*. University of Michigan Press.

Blatnický, M., Dižo, J., Gerlici, J., Sága, M., Lack, T., & Kuba, E. (2020). Design of a robotic manipulator for handling products of automotive industry. *International Journal of Advanced Robotic Systems, 17*(1), Article 1729881420906290. https://doi.org/10.1177/1729881420906290

Boresi, A. P., & Schmidt, R. J. (2001). *Engineering mechanics: Statics*. Brooks/Cole.

Carow, C., & Rackwitz, F. (2023). Cyclic compression of sands at constant stress ratio—experimental investigations and constitutive modelling. *Acta Geotechnica, 18*(3), 1305-1330. https://doi.org/10.1007/s11440-022-01628-z

Demishkevich, A., Thai, B. T., & Skonieczny, K. (2025). Advantages of slanted grousers for skid-steer planetary rovers with rigid wheels. *Mechatronics, 112*, Article 103408. https://doi.org/10.1016/j.mechatronics.2025.103408

Elsheikh, M. A. (2023). Design of a special rigid wheel for traversing loose soil. *Scientific Reports, 13*(1), Article 171. https://doi.org/10.1038/s41598-022-27312-6

Guo, J., Li, W., Ding, L., Gao, H., Guo, T., Huang, B., & Deng, Z. (2021). Linear expressions of drawbar pull and driving torque for grouser-wheeled planetary rovers without terrain mechanical parameters. *IEEE Robotics and Automation Letters, 6*(4), 8197-8204. https://doi.org/10.1109/lra.2021.3103641

Higa, S., Nagaoka, K., & Yoshida, K. (2019). Stress distributions of a grouser wheel on loose soil. *Journal of Terramechanics, 85*, 15-26. https://doi.org/10.1016/j.jterra.2019.07.001

Higa, S., Sawada, K., Nagaoka, K., Nagatani, K., & Yoshida, K. (2016). Measurement of stress distributions of a wheel with grousers traveling on loose soil. In *2016 IEEE International Conference on Robotics and Automation (ICRA)* (pp. 2828-2833). IEEE. https://doi.org/10.1109/icra.2016.7487445

Hruboš, M., Svetlík, J., Nikitin, Y., Pirník, R., Nemec, D., Šimák, V., Janota, A., Hrbček, J., & Gregor, M. (2016). Searching for collisions between mobile robot and environment. *International Journal of Advanced Robotic Systems, 13*(5), Article 1729881416667500. https://doi.org/10.1177/1729881416667500

Ibrahim, A. N., Aoshima, S., Shiroma, N., & Fukuoka, Y. (2016). The effect of assistive anchor-like grousers on wheeled rover performance over unconsolidated sandy dune inclines. *Sensors, 16*(9), Article 1507. https://doi.org/10.3390/s16091507

Ibrahim, A. N., & Fukuoka, Y. (2018). Effect of assistive grouser mechanism on lightweight rover power consumption pattern on steep soft sand inclines. In M. H. A. Hassan (Ed.), *Intelligent manufacturing & mechatronics* (pp. 343-351). Springer. https://doi.org/10.1007/978-981-10-8788-2_30

Ishikawa, T., Zhang, Y., Tokoro, T., & Miura, S. (2014). Medium-size triaxial apparatus for unsaturated granular subbase course materials. *Soils and Foundations, 54*(1), 67-80. https://doi.org/10.1016/j.sandf.2013.12.007

Kelemenová, T., Dovica, M., Božek, P., Koláriková, I., Benedik, O., Virgala, I., Prada, E., Miková, Ľ., Kot, T., & Kelemen, M. (2020). Specific problems in measurement of coefficient of friction using variable incidence tribometer. *Symmetry, 12*(8), Article 1235. https://doi.org/10.3390/sym12081235

Liu, J., Liu, X., Zhang, X., Chen, X., Li, H., Luan, L., Ding, C., & Gao, X. (2024). Experimental study on reinforcement of bionic grouser of deep-sea mining vehicle. *Biogeotechnics, 2*(3), Article 100088. https://doi.org/10.1016/j.bgtech.2024.100088

Nakamura, H., Nagaoka, K., & Yoshida, K. (2020). Soil flow analysis for grouser wheels based on a particle image velocimetry method. *Journal of Terramechanics, 91*, 233-241. https://doi.org/10.1016/j.jterra.2020.07.001

Onur, M. İ., Tuncan, M., & Tuncan, A. (2014). An experimental study for determining the shear modulus of Toyoura sand. In *Proceedings of the Second European Conference on Earthquake Engineering and Seismology* (Paper 829). https://eaee.org/Media/Default/2ECCES/2ecces_eaee/829.pdf

Qazizada, M. E., & Pivarčiová, E. (2016). Mobile robot controlling possibilities of inertial navigation system. *Procedia Engineering, 149*, 404-413. https://doi.org/10.1016/j.proeng.2016.06.685

Rubio, F., Valero, F., & Llopis-Albert, C. (2019). A review of mobile robots: Concepts, methods, theoretical framework, and applications. *International Journal of Advanced Robotic Systems, 16*(2), Article 1729881419839596. https://doi.org/10.1177/1729881419839596

Sabarudin, S. S., Ibrahim, A. N., & Fukuoka, Y. (2020a). Effect of grouser angle of attack on performance of adjustable robot wheel assistive grouser. In M. Osman Zahid, R. Abd. Aziz, A. Yusoff, N. Mat Yahya, F. Abdul Aziz, & M. Yazid Abu (Eds.), *iMEC-APCOMS 2019* (pp. 605-610). Springer. https://doi.org/10.1007/978-981-15-0950-6_92

Sabarudin, S. S., Ibrahim, A. N., & Fukuoka, Y. (2020b). Investigation of effect of assistive grouser attack angle when moving in unconsolidated soft sand inclination slope using discrete element method (DEM) simulation. In *2020 IEEE Student Conference on Research and Development (SCOReD)* (pp. 149-153). IEEE. https://doi.org/10.1109/scored50371.2020.9250997

Safdar, M., Newson, T., & Shah, F. (2021). Consolidated drained (CID) behavior of fibre reinforced cemented Toyoura sand in triaxial loading conditions. *International Journal of Geo-Engineering, 12*, Article 27. https://doi.org/10.1186/s40703-021-00165-0

Sakayori, G., & Ishigami, G. (2024). Modeling of slip rate-dependent traversability for path planning of wheeled mobile robot in sandy terrain. *Frontiers in Robotics and AI, 11*, Article 1320261. https://doi.org/10.3389/frobt.2024.1320261

Schäfer, B., Gibbesch, A., Krenn, R., & Rebele, B. (2010). Planetary rover mobility simulation on soft and uneven terrain. *Vehicle System Dynamics, 48*(1), 149-169. https://doi.org/10.1080/00423110903243224

Sutoh, M., Yusa, J., Ito, T., Nagatani, K., & Yoshida, K. (2012). Traveling performance evaluation of planetary rovers on loose soil. *Journal of Field Robotics, 29*(4), 648-662. https://doi.org/10.1002/rob.21405

Suzuki, H., Watanabe, Y., Kobayashi, T., Iagnemma, K., & Ozaki, S. (2020). Terramechanics-based investigation of grouser shape for rigid wheels: Comparison between rectangular and trapezoidal grousers. *Cogent Engineering, 7*(1), Article 1846254. https://doi.org/10.1080/23311916.2020.1846254

Tagliavini, L., Colucci, G., Botta, A., Cavallone, P., Baglieri, L., & Quaglia, G. (2022). Wheeled mobile robots: State of the art overview and kinematic comparison among three omnidirectional locomotion strategies. *Journal of Intelligent & Robotic Systems, 106*(3), Article 57. https://doi.org/10.1007/s10846-022-01745-7

Tapia, F., Santucci, S., & Géminard, J. C. (2016). Fracture reveals clustering in cohesive granular matter. *EPL (Europhysics Letters), 115*(6), Article 64001. https://doi.org/10.1209/0295-5075/115/64001

Treers, L. K., Cao, C., & Stuart, H. S. (2021). Granular resistive force theory implementation for three-dimensional trajectories. *IEEE Robotics and Automation Letters, 6*(2), 1887-1894. https://doi.org/10.1109/lra.2021.3057052

Watanabe, Y., Nakano, S., Suzuki, H., & Ozaki, S. (2023). Numerical analysis of wheel locomotion on soft soil using the extended terramechanics model based on cellular automata. *Journal of Terramechanics, 109*, 9-20. https://doi.org/10.1016/j.jterra.2023.05.005

Wong, J. Y. (1997). Dynamics of tracked vehicles. *Vehicle System Dynamics, 28*(2-3), 197-219. https://doi.org/10.1080/00423119708969354

Yokoyama, A., Nakashima, H., Shimizu, H., Miyasaka, J., & Ohdoi, K. (2020). Effect of open spaces between grousers on the gross traction of a track shoe for lightweight vehicles analyzed using 2D DEM. *Journal of Terramechanics, 90*, 31-40. https://doi.org/10.1016/j.jterra.2019.10.004

Zhang, W., Lyu, S., Xue, F., Yao, C., Zhu, Z., & Jia, Z. (2022). Predict the rover mobility over soft terrain using articulated wheeled bevameter. *IEEE Robotics and Automation Letters, 7*(4), 12062-12069. https://doi.org/10.1109/lra.2022.3211153